CubeSat Attitude Determination via Kalman Filtering of Magnetometer and Solar Cell Data

Erik P. Babcock
(ebabcoc2@illinois.edu)

Prof. Timothy Bretl, Faculty Advisor
University of Illinois, Urbana-Champaign

Attitude determination options are limited on a CubeSat due to power, mass, and volume constraints. This report documents the design and implementation of an extended Kalman filter (EKF) for attitude estimation using three-axis magnetometer and two-axis solar cell measurements. The motivation for such a system is to utilize sensors already present on most CubeSats, namely three-axis magnetometers for active magnetic detumbling and four faces of solar cell arrays for power generation. The system is developed and simulation-tested on a 1-U CubeSat in a 600 km dawn-dusk orbit. Results show the system can converge to an attitude accuracy of 2.5° within 1 orbit after detumbling.

I. INTRODUCTION

THE CubeSat standard provides industry and academia with a unique, low-cost opportunity to design, build, and fly picosatellites. As CubeSat technology advances, proposed scientific payloads become more sophisticated and often require improved attitude determination and control (ADC). Meeting these requirements is nontrivial because typical high-precision satellite ADC solutions, such as reaction wheels or star trackers, may not fit a CubeSat's power, mass, volume, or monetary budgets. This report tackles half of the problem: attitude determination.

The goal is to produce an EKF capable of estimating attitude on a dawn-dusk orbit to an accuracy of 2.5° using only three-axis magnetometer and two-axis solar cell measurements. Specifically, the solar cells are aligned normal to the $\pm x$ and $\pm y$ CubeSat body-fixed directions so that the $\pm z$ faces may be reserved for payload sensors, as shown in Fig. 1. The EKF must be able to converge from any initial attitude error given a maximum initial rate uncertainty of 0.7 deg/s, which corresponds to a conservative B-dot control settling velocity.[1]

Many CubeSats already use three-axis magnetometers for sensing during detumbling and four faces of solar cell arrays for power generation. Thus, the proposed method eliminates the need for further attitude sensors (such as sun sensors, horizon sensors, or star trackers) at the cost of increasing computational complexity.

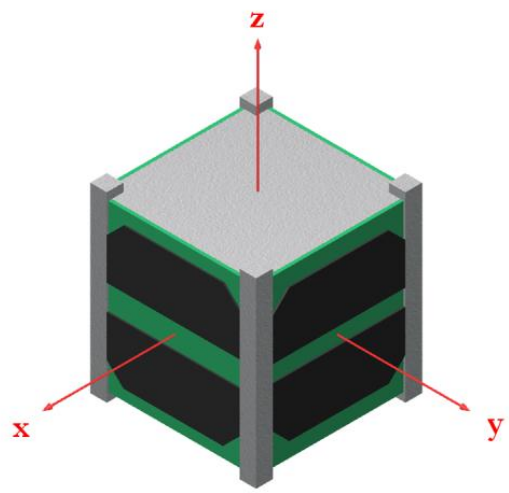

Figure 1. A typical 1-U CubeSat, with solar cells normal to the $\pm x$ and $\pm y$ CubeSat body-fixed directions

Psiaki et al presented an EKF that used only three-axis magnetometer data to determine attitude.[2] The system was able to converge from initial attitude errors as large as 60° to a 1-σ accuracy of 1°. To increase the initial error from which the EKF can converge, this report increases the sample rate from 50 samples per orbit to 1 sample per 10 sec. This 0.1 Hz rate is on the order of a typical active magnetic control cycle.[1]

Psiaki et al also noted that, on an 8 MHz processor, each filter time step took about 0.28 sec to compute, not including the time to compute a

magnetic field model from a spherical expansion. In contrast, recent CubeSats, such as CanX-2, have flown with processors capable of running at 40 MHz.[3] Therefore, using the additional solar cell measurements, it is reasonable to expect a similar EKF to run onboard at 0.1 Hz in flight.

Solar cell currents can provide a measure of the angle between incoming sunlight and a vector normal to the solar cell.[4] Therefore, with four panels, as shown in Fig. 1, two dimensions of the Sun's relative position may be resolved. This provides the extra information necessary for the EKF to converge from any initial attitude estimate, given a sufficiently small initial rate.

II. SPACECRAFT DYNAMIC MODEL

This report uses two right-handed reference frames. The ECI frame has its origin fixed at Earth's center. Its z axis passes through the North Pole and the x axis points to some inertial reference, such as the First Point of Aries. The $BODY$ frame has its origin at the CubeSat center of mass. The $BODY$ frame axes are in the directions of the principal moments of inertia, as seen in Fig. 1.

Attitude is represented with quaternions. $\boldsymbol{q} = [q_1, q_2, q_3, q_4]^T$ is a quaternion that rotates a vector in the coordinates of the $BODY$ frame into the coordinates of the ECI frame according to Eq.(1) below.[5]

$\boldsymbol{r}^{ECI}$ and $\boldsymbol{r}^{BODY}$ are vectors in ECI and $BODY$ coordinates, respectively. Note that the quaternion notation in this report treats q_1 as the scalar component.

The quaternion rate of change is

$$\dot{\boldsymbol{q}} = \frac{1}{2}\begin{bmatrix} -q_2 & -q_3 & -q_4 \\ q_1 & -q_4 & q_3 \\ q_4 & q_1 & -q_2 \\ -q_3 & q_2 & q_1 \end{bmatrix}\begin{bmatrix} \omega_1 \\ \omega_2 \\ \omega_3 \end{bmatrix} = \frac{1}{2}\boldsymbol{\Xi}(\boldsymbol{q})\boldsymbol{\omega} \qquad (2)$$

where $\boldsymbol{\omega} = [\omega_1, \omega_2, \omega_3]^T$ is the angular velocity of the $BODY$ frame with respect to ECI in the coordinates of the $BODY$ frame.

Eq.(2) is equivalent to

$$\dot{\boldsymbol{q}} = \frac{1}{2}\begin{bmatrix} 0 & -\omega_1 & -\omega_2 & -\omega_3 \\ \omega_1 & 0 & \omega_3 & -\omega_2 \\ \omega_2 & -\omega_3 & 0 & \omega_1 \\ \omega_3 & \omega_2 & -\omega_1 & 0 \end{bmatrix}\boldsymbol{q} = \frac{1}{2}\boldsymbol{\Omega}(\boldsymbol{\omega})\boldsymbol{q} \qquad (3)$$

Both representations of the quaternion derivative will be useful in defining the EKF.

The angular acceleration is provided by Euler's equations,

$$\dot{\boldsymbol{\omega}} = \boldsymbol{J}^{-1}\left(\boldsymbol{\tau} - \boldsymbol{\omega} \times (\boldsymbol{J}\boldsymbol{\omega})\right) \qquad (4)$$

where $\boldsymbol{J}$ is the spacecraft's inertia matrix and $\boldsymbol{\tau}$ is the sum of all external torques on the spacecraft in the coordinates of the $BODY$ frame.[6] External torques include gravity gradient, aerodynamic, solar pressure, and residual magnetic torques. The EKF developed in this report assumes torque-free motion to simplify the equations and analysis. However, adding predictable torques to the model, such as gravity gradient, would yield higher fidelity for onboard attitude determination.

III. SENSOR MODEL

Three-Axis Magnetometer

The three-axis magnetometer measures the local magnetic field according to

$$\boldsymbol{b}^{BODY} = \boldsymbol{A}^T\boldsymbol{b}^{ECI} \qquad (5)$$

where $\boldsymbol{b}^{BODY}$ is the local magnetic field in $BODY$ coordinates and $\boldsymbol{b}^{ECI}$ is the local magnetic field in ECI coordinates. In the EKF, the measurement will be compared to an expected value, which is computed from a magnetic field model, such as the International Geomagnetic Reference Field (IGRF). This expected local magnetic field requires both an expected attitude and position. Therefore, orbit

$$\boldsymbol{r}^{ECI} = \begin{bmatrix} q_1^2 + q_2^2 - q_3^2 - q_4^2 & 2(q_2q_3 - q_1q_4) & 2(q_2q_4 + q_1q_3) \\ 2(q_2q_3 + q_1q_4) & q_1^2 - q_2^2 + q_3^2 - q_4^2 & 2(q_3q_4 - q_1q_2) \\ 2(q_2q_4 - q_1q_3) & 2(q_3q_4 + q_1q_2) & q_1^2 - q_2^2 - q_3^2 + q_4^2 \end{bmatrix}\boldsymbol{r}^{BODY} = \boldsymbol{A}\boldsymbol{r}^{BODY} \qquad (1)$$

propagation is required in this scheme. Specific propagator algorithms are not investigated in this report. Instead, the simulations in the results section apply position knowledge errors on the order of propagators studied in other reports.

Solar Cells

The current generated by a solar cell can be modeled as

$$I_\alpha = I_{\alpha=0} cos\alpha \tag{6}$$

where I_α is the short circuit current at sun angle α and $I_{\alpha=0}$ is the short circuit current at a zero sun angle.[5] The sun α angle is illustrated in Fig. 2.

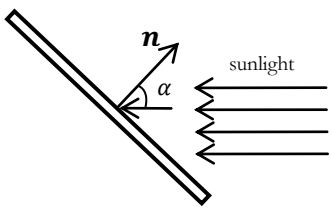

Figure 2. Sun angle definition

Other variables, such as temperature, can affect the solar cell's i-v curve. Also, exposure to space radiation will reduce performance.[6] This report continues using the model of Eq.(6) with the understanding that, in practice, the temperature and performance decay would have to be characterized and modeled by the spacecraft developer. For these reasons, a relatively large noise is applied to the solar cell measurements in simulation.

Consider a unit vector $\boldsymbol{s}^{BODY}$ that points from the Sun to the spacecraft and is in the coordinates of the $BODY$ frame. Then, if a CubeSat had solar cells on all six faces,

$$\boldsymbol{s}^{BODY} = \sum_{\substack{i=1 \\ \boldsymbol{s}^{BODY}\cdot\boldsymbol{n}_i < 0}}^{6} \boldsymbol{n}_i \, cos\alpha_i \tag{7}$$

where i indexes the faces of the spacecraft, $\boldsymbol{n}_i$ is the outward unit normal vector to face i in the coordinates of the $BODY$ frame, and α_i is the sun angle on face i. The $\boldsymbol{s}^{BODY} \cdot \boldsymbol{n}_i < 0$ constraint enforces that only faces in direct sunlight are accounted for.

The CubeSat in consideration can only resolve two dimensions of $\boldsymbol{s}^{BODY}$, the sun vector, since it does not have any solar cells normal to the $BODY$ z axis. Therefore, by Eq.(6) and Eq.(7), the solar cells produce the measurement

$$\boldsymbol{s}_{1-2}^{BODY} = \boldsymbol{A}_{1-2}^{T} \boldsymbol{s}^{ECI} \tag{8}$$

where $\boldsymbol{s}^{BODY}$ is the sun vector in $BODY$ coordinates and $\boldsymbol{s}^{ECI}$ is the sun vector in the ECI coordinates. The (1-2) subscript indicates only the first and second rows are included. As with the magnetometer measurement, the solar cell measurement will be compared to an expected value computed from a sun model. Again, the model requires the expected position and attitude of the spacecraft.

IV. SEVEN-DIMENSIONAL FILTER

In this section, a brute-force continuous-discrete extended Kalman filter is generated using all four quaternion coordinates.

The state vector is

$$\boldsymbol{x}(t) = [\boldsymbol{q}(t)^T, \boldsymbol{\omega}(t)^T]^T \tag{9}$$

and dynamics of the uncontrolled system are

$$\dot{\boldsymbol{x}}(t) = \boldsymbol{f}\big(\boldsymbol{x}(t)\big) + \boldsymbol{w}(t) \tag{10}$$

where t is time and $\boldsymbol{w}(t) \sim N(\boldsymbol{0}, \boldsymbol{Q})$ is the zero mean Gaussian process noise. In general, $\boldsymbol{f}$ would also depend on some control input $\boldsymbol{u}(t)$, but this report focuses only on determination. From Eqs. (2-4),

$$\boldsymbol{f}(\boldsymbol{x}) = \begin{bmatrix} f_1(\boldsymbol{x}) \\ \vdots \\ f_7(\boldsymbol{x}) \end{bmatrix} = \begin{bmatrix} \frac{1}{2}\Xi(\boldsymbol{q})\boldsymbol{\omega} \\ -\boldsymbol{J}^{-1}\big(\boldsymbol{\omega} \times (\boldsymbol{J}\boldsymbol{\omega})\big) \end{bmatrix} = \begin{bmatrix} \frac{1}{2}\boldsymbol{\Omega}(\boldsymbol{\omega})\boldsymbol{q} \\ -\boldsymbol{J}^{-1}(\boldsymbol{\omega} \times (\boldsymbol{J}\boldsymbol{\omega})) \end{bmatrix} \tag{11}$$

Thus, the state transition matrix is

$$\boldsymbol{F} = \frac{\partial \boldsymbol{f}(\boldsymbol{x})}{\partial \boldsymbol{x}} = \begin{bmatrix} \frac{1}{2}\boldsymbol{\Omega}(\boldsymbol{\omega}) & \frac{1}{2}\Xi(\boldsymbol{q}) \\ \boldsymbol{O}_{3x4} & \boldsymbol{\Pi}(\boldsymbol{\omega}) \end{bmatrix} \tag{12}$$

where $\boldsymbol{O}_{3x3}$ is a 3x3 zero matrix and

$$\boldsymbol{\Pi}(\boldsymbol{\omega}) = \frac{\partial \dot{\boldsymbol{\omega}}}{\partial \boldsymbol{\omega}} = \begin{bmatrix} 0 & \frac{J_2 - J_3}{J_1}\omega_3 & \frac{(J_2 - J_3)}{J_1}\omega_2 \\ \frac{J_3 - J_1}{J_2}\omega_3 & 0 & \frac{J_3 - J_1}{J_2}\omega_1 \\ \frac{J_1 - J_2}{J_3}\omega_2 & \frac{J_1 - J_2}{J_3}\omega_1 & 0 \end{bmatrix} \tag{13}$$

The measurement vector is

$$\boldsymbol{z}(t_k) = \boldsymbol{h}\big(\boldsymbol{x}(t_k)\big) + \boldsymbol{v}(t_k) \tag{14}$$

where t_k is the time of measurement k, $\boldsymbol{v}(t_k) \sim N(\boldsymbol{0}, \boldsymbol{R})$ is the observation noise, and $\boldsymbol{h}(\boldsymbol{x})$ is

$$\boldsymbol{h}(\boldsymbol{x}) = \begin{bmatrix} \frac{\boldsymbol{A}^T \boldsymbol{b}^{ECI}}{\|\boldsymbol{b}^{ECI}\|} \\ \boldsymbol{A}_{1-2}^T \boldsymbol{s}^{ECI} \end{bmatrix} \tag{15}$$

Note $\boldsymbol{h}(\boldsymbol{x})$ is just an augmented form of the magnetometer and solar cell measurements from Eqs. (5) and (8). Furthermore, $\boldsymbol{s}^{ECI}$ was defined as a unit vector, but $\boldsymbol{b}^{ECI}$ was not. The magnitude of $\boldsymbol{b}^{ECI}$ contains no attitude information, so it is normalized for consistency.

The innovation vector, $\boldsymbol{y}(t_k)$, compares the measured magnetic field and sun vector to the expected magnetic field and sun vector, according to

$$\boldsymbol{y}(t_k) = \boldsymbol{z}(t_k) - \boldsymbol{h}\big(\hat{\boldsymbol{x}}^-(t_k)\big) \tag{16}$$

where the $(\hat{\ })$ overstrike, as in $\hat{\boldsymbol{x}}$, indicates an estimate and the $(^-)$ superscript indicates a preupdate estimate, whereas the $(^+)$ superscript indicates a measurement-updated estimate. The observation matrix is

$$\begin{aligned} \boldsymbol{H}(t_k) &= -\frac{\partial \boldsymbol{y}(t_k)}{\partial \hat{\boldsymbol{x}}(t_k)} = \frac{\partial \boldsymbol{h}\big(\hat{\boldsymbol{x}}^-(t_k)\big)}{\partial \hat{\boldsymbol{x}}(t_k)} \\ &= \begin{bmatrix} \frac{\partial \boldsymbol{h}\big(\hat{\boldsymbol{x}}^-(t_k)\big)}{\partial \hat{\boldsymbol{q}}(t_k)} & \boldsymbol{O}_{5x3} \end{bmatrix} \\ &= \begin{bmatrix} \boldsymbol{\Theta}\big(\hat{\boldsymbol{q}}(t_k)\big) & \boldsymbol{O}_{5x3} \end{bmatrix} \end{aligned} \tag{17}$$

where

$$\boldsymbol{\Theta}(\hat{\boldsymbol{q}}) = \begin{bmatrix} \frac{\partial \hat{\boldsymbol{A}}^T}{\partial \hat{q}_1} \frac{\hat{\boldsymbol{b}}^{ECI}}{\|\hat{\boldsymbol{b}}^{ECI}\|} & \cdots & \frac{\partial \hat{\boldsymbol{A}}^T}{\partial \hat{q}_4} \frac{\hat{\boldsymbol{b}}^{ECI}}{\|\hat{\boldsymbol{b}}^{ECI}\|} \\ \frac{\partial \hat{\boldsymbol{A}}_{1-2}^T}{\partial \hat{q}_1} \hat{\boldsymbol{s}}^{ECI} & \cdots & \frac{\partial \hat{\boldsymbol{A}}_{1-2}^T}{\partial \hat{q}_4} \hat{\boldsymbol{s}}^{ECI} \end{bmatrix} \tag{18}$$

with the rotation matrix $\boldsymbol{A}$ defined in terms of $\boldsymbol{q}$, as in Eq. (1). The rotation matrix partial derivatives are

$$\frac{\partial \boldsymbol{A}^T}{\partial q_1} = 2\begin{bmatrix} q_1 & q_4 & -q_3 \\ -q_4 & q_1 & q_2 \\ q_3 & -q_2 & q_1 \end{bmatrix} \tag{19}$$

$$\frac{\partial \boldsymbol{A}^T}{\partial q_2} = 2\begin{bmatrix} q_2 & q_3 & q_4 \\ q_3 & -q_2 & q_1 \\ q_4 & -q_1 & -q_2 \end{bmatrix} \tag{20}$$

$$\frac{\partial \boldsymbol{A}^T}{\partial q_3} = 2\begin{bmatrix} -q_3 & q_2 & -q_1 \\ q_2 & q_3 & q_4 \\ q_1 & q_4 & -q_3 \end{bmatrix} \tag{21}$$

$$\frac{\partial \boldsymbol{A}^T}{\partial q_4} = 2\begin{bmatrix} -q_4 & q_1 & q_2 \\ -q_1 & -q_4 & q_3 \\ q_2 & q_3 & q_4 \end{bmatrix} \tag{22}$$

Combined, the above equations can be used together in a standard EKF:

Predict:

$$\dot{\hat{\boldsymbol{x}}}(t) = \boldsymbol{f}\big(\hat{\boldsymbol{x}}(t)\big) \quad with \quad \hat{\boldsymbol{x}}(t_{k-1}) = \hat{\boldsymbol{x}}^+(t_{k-1}) \tag{23}$$

$$\dot{\boldsymbol{P}}(t) = \boldsymbol{F}(t)\boldsymbol{P}(t) + \boldsymbol{P}(t)\boldsymbol{F}(t)^T + \boldsymbol{Q}(t) \quad with \quad \boldsymbol{P}(t_{k-1}) = \boldsymbol{P}^+(t_{k-1}) \tag{24}$$

Update:

$$\boldsymbol{K}(t_k) = \boldsymbol{P}^-(t_k)\boldsymbol{H}^T(t_k)[\boldsymbol{R} + \boldsymbol{H}(t_k)\boldsymbol{P}^-(t_k)\boldsymbol{H}^T(t_k)]^{-1} \tag{25}$$

$$\hat{\boldsymbol{x}}^+(t_k) = \hat{\boldsymbol{x}}^-(t_k) + \boldsymbol{K}(t_k)\boldsymbol{y}(t_k) \tag{26}$$

$$\boldsymbol{P}^+(t_k) = \big(\boldsymbol{I} - \boldsymbol{K}(t_k)\boldsymbol{H}(t_k)\big)\boldsymbol{P}^-(t_k) \tag{27}$$

However, the covariance matrix, $\boldsymbol{P} \in \mathbb{R}^{7x7}$, is singular because of the quaternion's unit norm constraint. This is numerically difficult to maintain and may result in negative eigenvalues. An alternative interpretation is that the filter attempts to correct errors in four attitude dimensions, but only three are independent. Lefferts et al notes this and presents a truncated representation of the covariance matrix to maintain singularity.[7] However, the equations in this section were not derived in vain, because they provide a basis for the truncated EKF, as shown in the following section.

V. TRUNCATED KALMAN FILTER

In order to avoid a singular covariance matrix $\boldsymbol{P}$, the entire filter may be truncated to six dimensions by choosing one of the quaternion components to be a dependent variable,

$$q_c = \pm\sqrt{1 - \sum_{\substack{i=1 \\ i\neq c}}^{4} q_i} \tag{28}$$

where c is the index of the dependent component.

It is useful to define the function

$$\eta(\bar{\imath}, c) = \begin{cases} \bar{\imath} & if \quad \bar{\imath} < c \\ \bar{\imath} + 1 & otherwise \end{cases} \tag{29}$$

$\eta(\bar{\imath}, c)$ defines the relationship between the indices of truncated vectors/matrices, $\bar{\imath}$, and the corresponding indices in the original vectors/matrices, $i = \eta(\bar{\imath}, c)$, given some chosen dependent quaternion coordinate with index c. The $(\bar{\ })$ overbar indicates a truncated expression or the index of a truncated expression. A left superscript indicates the index of the dependent quaternion component. For example, the truncated state is

$${}^{c}\overline{\boldsymbol{x}} = [{}^{c}\overline{\boldsymbol{q}}^{T}, \boldsymbol{\omega}^{T}]^{T} \tag{30}$$

where the ith component of ${}^{c}\overline{\boldsymbol{q}}$ is

$${}^{c}\bar{q}_{\bar{\imath}} = q_{\eta(\bar{\imath},c)} \qquad for\ \bar{\imath} = 1, 2, 3 \tag{31}$$

Similarly, the state rate of change is

$${}^{c}\dot{\overline{\boldsymbol{x}}} = {}^{c}\overline{\boldsymbol{f}}(\boldsymbol{x}(t)) + {}^{c}\overline{\boldsymbol{w}}(t) \tag{32}$$

Where the ith component of ${}^{c}\overline{\boldsymbol{f}}(\boldsymbol{x}(t))$ and ${}^{c}\overline{\boldsymbol{w}}(t)$ are

$${}^{c}\bar{f}_{\bar{\imath}}(\boldsymbol{x}(t)) = f_{\eta(\bar{\imath},c)}(\boldsymbol{x}(t)) \quad for\ \bar{\imath} = 1, \dots, 6 \tag{33}$$

and

$${}^{c}\bar{w}_{\bar{\imath}}(t) = w_{\eta(\bar{\imath},c)}(t) \quad for\ \bar{\imath} = 1, \dots, 6 \tag{34}$$

The remainder of this report assumes $i = \eta(\bar{\imath}, c)$ and $j = \eta(\bar{\jmath}, c)$.

The truncated filter matrices ${}^{c}\overline{\boldsymbol{H}}$ and ${}^{c}\overline{\boldsymbol{F}}$ must account for the dependence of the cth component of $\boldsymbol{q}$. From Eq.(28), the partial derivate of g, some arbitrary function of the quaternion, is

$$\begin{aligned} \frac{\partial}{\partial q_i} g({}^{c}\overline{\boldsymbol{q}},\ q_c({}^{c}\overline{\boldsymbol{q}})) &= \frac{\partial g}{\partial q_i} + \frac{\partial g}{\partial q_c}\left(\frac{\partial q_c}{\partial q_i}\right) \\ &= \frac{\partial g}{\partial q_i} - \frac{q_i}{q_c}\left(\frac{\partial g}{\partial q_c}\right) \quad for\ i \neq c \end{aligned} \tag{35}$$

Expressions for the truncated state transition and observation matrices can be derived from Eq.(35).

$${}^{c}\overline{\boldsymbol{F}} = \frac{\partial}{\partial {}^{c}\overline{\boldsymbol{x}}}\left({}^{c}\overline{\boldsymbol{f}}(\boldsymbol{x})\right) = \begin{bmatrix} \frac{1}{2}{}^{c}\overline{\boldsymbol{\Omega}} & \frac{1}{2}{}^{c}\overline{\boldsymbol{\Xi}} \\ \boldsymbol{O}_{3x3} & \boldsymbol{\Pi} \end{bmatrix} \tag{36}$$

where the elements of ${}^{c}\overline{\boldsymbol{\Omega}}$ are

$$[{}^{c}\overline{\boldsymbol{\Omega}}]_{\bar{\imath}\bar{\jmath}} = [\boldsymbol{\Omega}]_{i\,j} - \frac{q_j}{q_c}[\boldsymbol{\Omega}]_{i\,c} \qquad for\ \bar{\imath}, \bar{\jmath} = 1, 2, 3 \tag{37}$$

and the elements of ${}^{c}\overline{\boldsymbol{\Xi}}$ are

$$\left[{}^{c}\overline{\boldsymbol{\Xi}}\right]_{\bar{\imath}\,j} = [\boldsymbol{\Xi}]_{i\,j} \qquad for\ \bar{\imath}, j = 1, 2, 3 \tag{38}$$

The dimensions of the measurement $\boldsymbol{h}(\boldsymbol{x})$ are not changed by the truncation. The truncated observation matrix becomes

$${}^{c}\overline{\boldsymbol{H}} = \frac{\partial \boldsymbol{h}}{\partial {}^{c}\widehat{\overline{\boldsymbol{x}}}} = \left[{}^{c}\overline{\boldsymbol{\Theta}} \quad \boldsymbol{O}_{3x3}\right] \tag{39}$$

Where the elements of ${}^{c}\overline{\boldsymbol{\Theta}}$ are

$$\left[{}^{c}\overline{\boldsymbol{\Theta}}\right]_{i\,\bar{\jmath}} = [\boldsymbol{\Theta}]_{i\,j} - \frac{q_j}{q_c}[\boldsymbol{\Theta}]_{i\,c} \qquad for\ i = 1, \dots, 5 \quad and \quad \bar{\jmath} = 1, 2, 3 \tag{40}$$

The above equations for ${}^{c}\overline{\boldsymbol{x}}$, ${}^{c}\dot{\overline{\boldsymbol{x}}}$, ${}^{c}\overline{\boldsymbol{F}}$, and ${}^{c}\overline{\boldsymbol{H}}$ provide the tools necessary to implement the truncated EKF with a nonsingular ${}^{c}\overline{\boldsymbol{P}} \in \mathbb{R}^{6x6}$. The truncated EKF follows the same prediction and update steps of Eqs. (23-27), but in a lower dimension.

After each update step in the truncated EKF, the update for the full state quaternion, $\boldsymbol{q}^{+}(t_k)$, is simply a normalization,

$$q_i^{+}(t_k) = \begin{cases} \dfrac{q_i^{+}(t_k)}{\sqrt{q_c^{-}(t_k) + \sum_{\bar{i}=1}^{3} q_{\bar{i}}^{+}(t_k)}} & for\ i \neq c \\ \dfrac{q_i^{-}(t_k)}{\sqrt{q_c^{-}(t_k) + \sum_{\bar{i}=1}^{3} q_{\bar{i}}^{+}(t_k)}} & otherwise \end{cases} \tag{41}$$

Note from Eqs. (37) and (40) that a singularity exists for $q_c = 0$. This motivates the presented rigorous formulation of the truncated EKF in terms of a general quaternion index c. To estimate $\boldsymbol{q}(t)$, the choice of dependent quaternion component may have to change with time to avoid the aforementioned singularity. This is accomplished via the heuristic

$$c(t_k) = \underset{i}{argmax} |q_i^{-}(t_k)| \tag{42}$$

If c changes, the truncated covariance ${}^{c}\overline{\boldsymbol{P}}$ must also be updated to account for the change in the chosen dependent quaternion. The original covariance $\boldsymbol{P} \in \mathbb{R}^{7x7}$ can be recovered from the truncated covariance ${}^{c}\overline{\boldsymbol{P}} \in \mathbb{R}^{6x6}$ according to [7]

$$[\boldsymbol{P}]_{c\,j} = -\frac{1}{\hat{q}_c} \sum_{i=1}^{3} {}^{c}\hat{\overline{q}}_i [{}^{c}\overline{\boldsymbol{P}}]_{i\,\bar{j}} \tag{43}$$

and

$$[\boldsymbol{P}]_{c\,c} = \frac{1}{|\hat{q}_c|^2} \sum_{i=1}^{3} \sum_{i=1}^{3} {}^{c}\hat{\overline{q}}_i [{}^{c}\overline{\boldsymbol{P}}]_{i\,j}\, {}^{c}\hat{\overline{q}}_j \tag{44}$$

VI. SIMULATION-TESTING

The piecewise nature of the filter and nonlinearities in the system make an analytical analysis of the presented EKF difficult. Therefore, simulation testing is used to characterize the filter. Each simulation has four parts, each of which successively calculates variables of interest, as listed below.

Orbit Simulation

- $\boldsymbol{r}^{ECI}(t)$, the position of the spacecraft in ECI
- $\boldsymbol{r}_{Sun}^{ECI}(t)$, the position of the Sun in ECI

Attitude Simulation

- $\boldsymbol{x}(t)$, the 7-dimensional state, as in Eqs. (9) and (10), accounting for gravity gradient torque

Sensor Data Simulation

- $\hat{\boldsymbol{r}}^{ECI} = \hat{\boldsymbol{r}}^{ECI}(\boldsymbol{r}^{ECI}, \sigma_{prop})$, the propagated position
- $\boldsymbol{s}^{ECI} = \boldsymbol{s}^{ECI}(\boldsymbol{r}^{ECI}, \boldsymbol{r}_{Sun}^{ECI})$, the true Sun vector in ECI
- $\hat{\boldsymbol{s}}^{ECI} = \hat{\boldsymbol{s}}^{ECI}(\hat{\boldsymbol{r}}^{ECI}, \boldsymbol{r}_{Sun}^{ECI}, \sigma_{Sun})$, the expected Sun vector in ECI
- $\boldsymbol{s}_{1-2,meas}^{BODY} = \boldsymbol{s}_{1-2,meas}^{BODY}(\boldsymbol{q}, \boldsymbol{s}^{ECI}, \sigma_{solar})$, the sensed Sun vector
- $\boldsymbol{b}^{ECI} = \boldsymbol{b}^{ECI}(\boldsymbol{r}^{ECI})$, the true local magnetic field in ECI
- $\hat{\boldsymbol{b}}^{ECI} = \hat{\boldsymbol{b}}^{ECI}(\hat{\boldsymbol{r}}^{ECI}, \sigma_{IRGF})$, the expected local magnetic field in ECI
- $\boldsymbol{b}_{meas}^{BODY} = \boldsymbol{b}_{meas}^{BODY}(\boldsymbol{q}, \boldsymbol{b}^{ECI}, \sigma_{mag})$, the sensed local magnetic field

Filter Simulation

- $\hat{\boldsymbol{x}} = \hat{\boldsymbol{x}}(\hat{\boldsymbol{x}}_0,\ \boldsymbol{s}_{meas}^{BODY}, \hat{\boldsymbol{s}}^{ECI}, \boldsymbol{b}_{meas}^{BODY}, \boldsymbol{b}^{ECI})$, the estimated state

The simulations include a downrange propagator bias ($p_{prop,dr}$), and zero-bias Gaussian noise for the orbit propagation (σ_{prop}), sun model inaccuracies (σ_{Sun}), IGRF model inaccuracies

(σ_{IGRF}), solar cell noise (σ_{solar}), and magnetometer noise (σ_{mag}). The values used are listed in Table 1.

Table 1. Simulated Gaussian Noise

Noise Source	Value
$p_{prop,dr}$ [km]	4.0
σ_{prop} [km]	2.0
σ_{Sun} [deg]	0.01
σ_{solar} [deg]	15
σ_{IGRF} [nT]	20
σ_{mag} [nT]	25

The propagator error is chosen based on Simplified General Perturbations model 4 (SGP4) errors for an approximate 2 day period.[8] The Sun model error is based on "low precision" ephemeris data.[9] The solar cell angular noise is roughly based on Santoni and Bolotti data, with additional inaccuracies added to account for temperature fluctuations and decayed performance.[4] IGRF model error is based on the model's suggested root mean square vector error averaged over Earth's surface.[10] Magnetometer noise is based on commercially available hardware.

Furthermore, additional errors are intentionally introduced with the attitude dynamics simulator. The attitude dynamics are simulated with 2% mass error and 1.5° principle axes skew (about each axis) relative to the inertia matrix programmed in the EKF. Also, gravity gradient torque,

$$\boldsymbol{\tau}_{gg} = \frac{3\mu}{\|\boldsymbol{r}\|^5}\boldsymbol{r} \times \boldsymbol{J}\boldsymbol{r} \tag{45}$$

is simulated to test the filter's response to unmodeled external torques. μ is Earth's standard gravitational parameter, $\boldsymbol{J}$ is the spacecraft's inertia matrix, and $\boldsymbol{r}$ is the spacecraft's position. Gravity gradient torque was chosen for both its ease in modeling and because it is on the same order of magnitude as other worst case disturbances for 1-U CubeSat in a 600km orbit.[2]

Table 2. Worst Case Disturbance Torques

Disturbance Torque	Magnitude [N · m]
Aerodynamic	6.97 e – 9
Gravity Gradient	1.75 e – 9
Solar Pressure	1.64 e – 9

VII. RESULTS

The simulation parameters tested are summarized in Table 2. The initial attitude is chosen to be aligned with ECI. The magnitude of the initial angular velocity is based on a conservative settling rate of 0.7 deg/s after active magnetic detumbling.

Table 3. Simulation Inputs

Input	Value
$\boldsymbol{q}(t=0)$	$[1, 0, 0, 0]^T$
$\boldsymbol{\omega}(t=0)$ [deg/s]	$[0.5, 0.5, 0.5]^T$
J_{11} [kg · m²]	0.0017
J_{22} [kg · m²]	0.0015
J_{33} [kg · m²]	0.0020

The principal moments of inertia are those programmed in the filter and are roughly based on an even mass distribution. The difference between the maximum and minimum moments is based on the CP2 solid model with a safety factor of 2.5.[1] This factor is applied to increase the magnitude of gravity gradient disturbance torques, thus further testing the filter's robustness.

Convergence

The EKF must be able to converge from any initial attitude error, given a sufficiently small initial angular rate, since it is assumed that no attitude information will be available during or after active magnetic detumbling.

To empirically test the convergence requirements, the EKF was tested using a set of initial attitude errors of 180°. These initial errors were sampled using an angle-axis rotation representation. Consider θ and ϕ, the azimuthal and polar angles measured with respect to the $BODY$ frame.

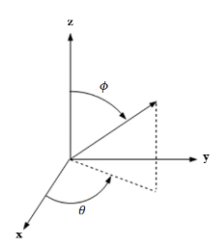

Figure 3. Azimuth and polar angles in $BODY$ frame

The rotational axes used to generate initial attitude errors were found by sampling $\theta \epsilon [0^\circ, 360^\circ)$ and $\phi \epsilon [0^\circ, 90^\circ)$ in 30° increments, as shown in Fig. 4.

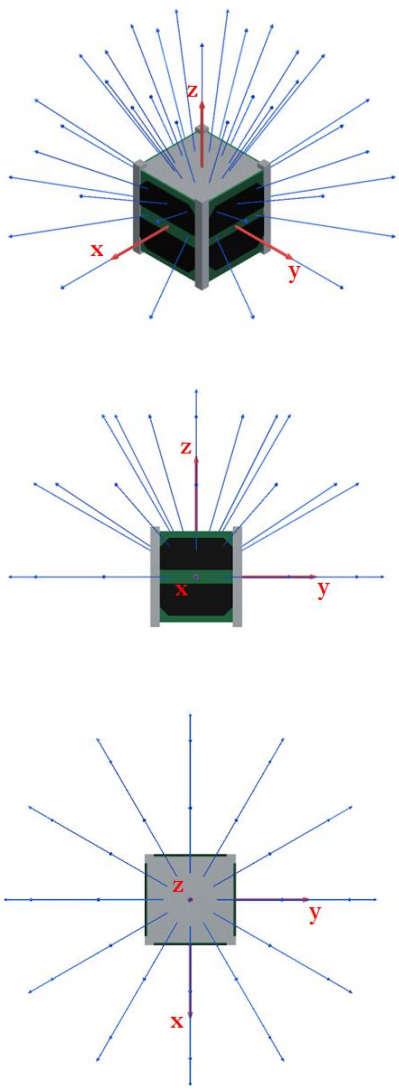

Figure 4. Sampled axes of rotation used to generate initial attitude errors of 180°

For each attitude/sensor simulation, 48 filter simulations were completed: each one initialized with a 180° rotation error about one of the rotational axes in Fig. 4.

The estimated attitude results for nominal noise levels are shown in Fig. 5. Each colored plot corresponds to the filtering of one of the 48 initial attitude errors.

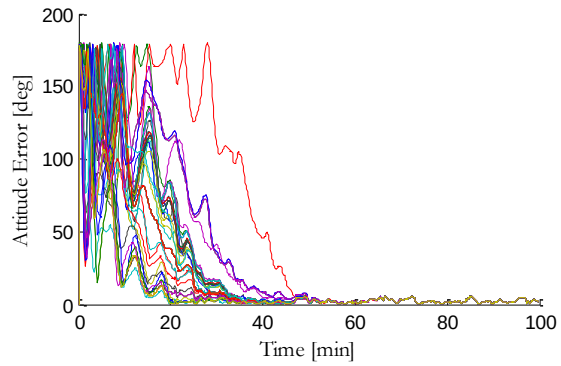

Figure 5. Convergence from 180° initial attitude error with nominal noise

The results provide empirical evidence that the proposed EKF can converge from any initial attitude, provided appropriate gains are selected. Furthermore, convergence is achieved within approximately one half of an orbit, or about 50 minutes. The nominal noise levels result in a converged pointing knowledge of 5°.

Accuracy

Further testing revealed that reducing the noise in the sun angle measurements resulted in more precise pointing knowledge. This makes intuitive sense because, unlike the magnetometer measurements, the sun angle measurements are almost negligibly affected by orbit propagation errors on the order of 6 km.

Figure 6 shows the convergence from the 48 initial attitude errors with only 10° standard deviation in measured sun angle noise. Notice, again, the empirical evidence further suggests convergence from any initial attitude. The converged pointing knowledge was 4.5° in this case.

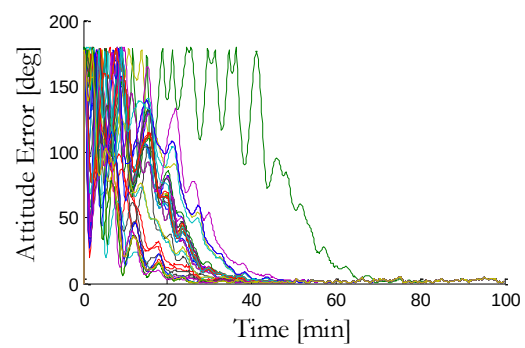

Figure 6. Convergence from 180° initial attitude error with σ_{solar}=10°

Figure 6 also provides an example of one of the potential drawbacks of an EKF: unexpected behavior resulting from nonlinearities. The green plot takes about 50% longer to converge than the others, although convergence is still achieved within one orbit.

A final set of filter simulations was completed with σ_{solar} = 5˚. The results are shown in Fig. 7.

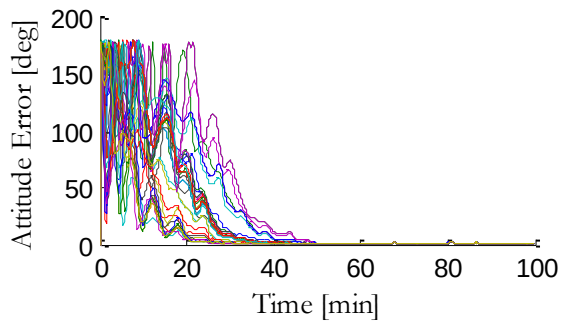

Figure 7. Convergence from 180˚ initial attitude error with σ_{solar}=5˚

This final reduction in σ_{solar} resulted in a converged pointing knowledge of 2.5˚. Again, simulations converged from all sampled initial 180˚ attitude errors.

VIII. CONCLUSIONS

An EKF was designed and simulation-tested to estimate attitude based on only three-axis magnetometer and two-axis solar cell measurements. Results empirically showed filter convergence within 60 minutes, or even half an orbit for many cases. The documented truncated EKF can conservatively provide attitude knowledge within 5˚. If the sun angle measurement noise is reduced to a 1-σ value of 5˚, attitude knowledge within 2. 5˚ is obtained.

The benefits of such an attitude determination system are numerous. The system is cost effective because it utilizes sensors already present on most CubeSats, thus eliminating the need for additional hardware. This also provides mass and volume savings, which can be used to support more payload applications. The system is robust because empirical evidence shows convergence from any initial attitude error.

Although only tested on a dawn-dusk orbit, this determination system may be applied in a hybrid fashion to orbits that pass through umbra. If convergence is achieved in half an orbit period while in sunlight, as in Fig. 7, a determination system that uses an EKF on only magnetometer measurements may be used when the solar cells reach darkness.

Future work is planned to analytically study the convergence and stability of the presented filter, although it is already clear that, given sufficient numerical simulation, this is a viable option for attitude determination on low-budget spacecraft.

ACKNOWLEDGMENTS

The IlliniSat project/course, led by Dr. Paul Scott Carney and Dr. David Carroll, at the University of Illinois provided the groundwork for this study. In particular, the ADC team, led by Erik Kroeker with support from Alex Ghosh, provided the motivation to push the envelope in attitude determination performance.

My thanks go out to Dr. Jordi Puig-Suari and his lab of student engineers for introducing me to the CubeSat community last summer. Your talents and accomplishments are remarkable, and I am very lucky to have been even a small part of your team.

Additionally, I owe thanks to the Guidance, Navigation, and Control team at SpaceX for giving me an opportunity to learn and work with them as they revolutionize spaceflight.

I would especially like to thank and acknowledge Dr. Timothy Bretl, to whom I can attribute most of my academic successes. His courses are always engaging, insightful, and well-thought. His collaboration far surpasses even that.

Finally, Kimberly Foster was an integral part in the brainstorming and review processes of this study. Her contributions made this report possible.

REFERENCES

[1]Guerrant, D. V., "Design and Analysis of Fully Magnetic Control for Picosatellite Stabilization," M.S. Thesis, Aerospace Engineering Dept., California Polytechnic State University, San Luis Obispo, CA, 2005.

[2]Psiaki, M. L., Martel, F., and Pal, P.K., "Three-Axis Attitude Determination via Kalman Filtering of Magnetometer Data," *Journal of Guidance, Control, and Dynamics,* Vol. 13, No. 3, 1989, pp. 506-514.

[3]Sarda, K., Grant, C., Eagleson, S., Kekez, D. D., Shah, A., Zee, R. E., "Canadian Advanced Nanospace Experiment 2 Orbit Operations: Two Years of Pushing the Nanosatellite Performance Envelope," *Small Satellite Conference,* No. SSC09-IV-6, AIAA/USU, Logan, UT, 2009.

[4]Santoni, F., Bolotti, F., "Attitude Determination of Small Spinning Spacecraft Using Three Axis Magnetometer and Solar Panels Data," *Aerospace Conference Proceedings,* Vol. 7, IEEE, Big Sky, MT, 2000, pp. 127-133.

[5]Wie, B., *Space Vehicle Dynamics and Control*, 1st ed, AIAA Education Series, AIAA, Reston, VA, 1998, pp. 307-331.

[6]M. A. Green, *Solar Cells Operating Principles, Technology and System Applications,* Centre for Photovoltaic Devices and Systems, University of NewSouth Wales, 1992.

[7]Lefferts, E. J., Markley, F.L., and Shuster, M.D., "Kalman Filtering for Spacecraft Attitude Estimation," *Journal of Guidance, Control and Dynamics*, Vol. 5, No. 5, Sept.-Oct. 1982, pp.417-429.

[8]Vallado, D. A., Crawford, P., Hujsak, R., Kelso, T. S.,. "Revisiting Spacetrack Report #3". *Astrodynamics Specialist Conference,* 2006.

[9]*The Astronomical Almanac*, U.S Government Printing Office , Washington, DC, 2005.

[10]Lowes, F. J.. "An estimate of the errors of the IGRF/DGRF fields 1945-2000," *Earth Planets Space*, Vol. 52, 2000, pp. 1207-1211.